# FeSi<sub>4</sub>P<sub>4</sub> and CoSi<sub>3</sub>P<sub>3</sub>: Hidden Gems of Ternary Tetrel Pnictides with Outstanding Nonlinear Optical Properties

Ernesto Soto, <sup>a,b</sup> Shannon J. Lee, <sup>a,b,c</sup> Andrew P. Porter, <sup>a,b</sup> Gayatri Viswanathan, <sup>a,b</sup> Georgiy Akopov, <sup>d</sup> Nethmi Hewage, <sup>a,b</sup> Kui Wu, <sup>e</sup> Victor Trinquet, <sup>f</sup> Guillaume Brunin, <sup>f</sup> Geoffroy Hautier, <sup>g</sup> Gian-Marco Rignanese, <sup>f</sup> Aaron J. Rossini, <sup>a,b</sup> and Kirill Kovnir\*<sup>a,b</sup>

<sup>a</sup> Department of Chemistry, Iowa State University, Ames, Iowa 50011, United States

<sup>b</sup> Ames National Laboratory, U.S. Department of Energy, Ames, Iowa 50011, United States

<sup>c</sup> Physical Science Division, Pacific Northwest National Laboratory, U.S. Department of Energy, Richland, Washington 99352, United States

<sup>d</sup> Department of Chemistry, Rutgers University, Newark, New Jersey 07102, United States

<sup>e</sup> State Key Laboratory of Crystal Materials and Institute of Crystal Materials, Shandong University, Jinan, 071002, China

<sup>f</sup> UCLouvain, Institute of Condensed Matter and Nanosciences (IMCN), Chemin des Étoiles 8, Louvain-la-Neuve B-1348, Belgium

<sup>g</sup> Thayer School of Engineering, Dartmouth College, Hanover, New Hampshire 03755, United States

Corresponding author e-mail: kovnir@iastate.edu

#### **Abstract**

Metal silicon phosphides have shown promise as nonlinear optical materials. To be practically useful and cheap, the materials of earth-abundant 3*d* transition metals are preferred over their scarcer and more expensive 4*d* and 5*d* counterparts. We developed a synthetic method to produce polycrystalline bulk powders and millimeter-sized single crystals of ternary compounds, FeSi<sub>4</sub>P<sub>4</sub> and CoSi<sub>3</sub>P<sub>3</sub>. Both studied compounds have noncentrosymmetric and chiral crystal structures with ordered Si/P arrangements as was confirmed by single crystal X-ray diffraction and solid-state NMR. Despite the presence of the transition metal, FeSi<sub>4</sub>P<sub>4</sub> and CoSi<sub>3</sub>P<sub>3</sub> are semiconductors with direct bandgaps of 1.3 eV and 1.6 eV, respectively, indicating low spin *d*<sup>6</sup> electronic configuration for octahedral Fe<sup>2+</sup> and Co<sup>3+</sup>. Relative to reported sulfides materials, FeSi<sub>4</sub>P<sub>4</sub> and CoSi<sub>3</sub>P<sub>3</sub> small bandgap semiconductors demonstrate an outstanding combination of second harmonic generation (SHG) activity and laser damage threshold (LDT). Both studied materials are phase-matchable with a 2.09 μm laser, and not only exhibit 2.5-3.0 times stronger SHG signal than that of the state-of-the-art AgGaS<sub>2</sub> standard, but also demonstrate, LDT response of 2.3-2.5 times higher than that of AgGaS<sub>2</sub> (at 1.09 μm laser with a pulse width of 10 ns) – which is unprecedented for small bandgap semiconductors.

#### Introduction

Development of materials with improved performance, a sustainable nature, and cheap and abundant components is the mainstream direction of current materials research. Nonlinear optical materials (NLO) are crucial for the optics field due to their ability to upconvert frequencies of incoming light. State-of-the-art NLO materials cover a significant part of the electromagnetic spectrum; however, there are still gaps including the infrared (IR) region (2-20 μm). IR-NLO materials are important due to their application in optoelectronic devices, resource exploration, and long-distance laser communication. <sup>1-5</sup>

For second harmonic generation activity, NLO materials must possess: (1) first and most crucial, non-centrosymmetric (NCS) crystal structure; (2) a semiconducting nature with suitable band gap for good transmission at the required spectrum region; (3) large second-harmonic generation (SHG) coefficients; and (4) high laser damage threshold (LDT).<sup>6-10</sup> Currently sulfides, such as AgGaS<sub>2</sub> and LiInSe<sub>2</sub>, are used for IR-NLO applications.<sup>11,12</sup> In sulfides, a general observed trend is that SHG is inversely proportional and LDT is directly proportional to the bandgap due to the polar nature of metal-chalcogen bonds, which prevents properties optimization by simply adjusting the bandgap.

A paradigm-shift approach to IR-NLO materials was recently offered by studies of metal tetrel-pnictides (tetrel, *Tt*: Group 14 element such as Si, Ge; pnictogen, *Pn*: group 15 elements such as P, As). <sup>13-17</sup> The presence of two non-metal elements, like Si and P, with diverse bonding modes allows for the realization of noncentrosymmetric (NCS) structures for alkali-earth and rare-earth metal cations. <sup>14-21</sup> NCS structures are crucial for realizing properties such as piezoelectricity, pyroelectricity, chiral magnetism, and superconductivity. <sup>22</sup> When considering alkali, alkaline-earth, and rare-earth tetrel-pnictides, the electropositive metal cation is surrounded by the most electronegative pnictogen atoms and the nature of the metal-pnictogen interaction is essentially ionic. In ternary tetrel pnictides with a group of 8-11 transition metals, an assortment of crystal structures is formed with a mixture of covalent metal-pnictogen and metal-tetrel interactions. <sup>13,16,23,24</sup> The only exception is chalcopyrite MnSiP<sub>2</sub> which does not have Mn-Si bonding. <sup>13</sup> In general, NCS metal tetrel pnictides exhibit a substantial combination of SHG and LDT. <sup>25,26</sup>

By analyzing several transition metal silicon phosphides (M-Si-P), we hypothesized that the more electropositive nature of Si leads to the  $\pi$ -electron back donation between the filled d-orbitals of the transition metal and the empty antibonding Si-P orbitals, which is more effective than the  $\pi$ electron back donation between M and P.<sup>24</sup> These bonding preferences stabilize NCS local fragments such as linear Si-M-P, cis-MSi<sub>2</sub>P<sub>4</sub>, and fac-MSi<sub>3</sub>P<sub>3</sub> units. 16,24,27 Similar trends were observed for heavier tetrel-pnictides, with cis-MTt<sub>2</sub>As<sub>2</sub> and fac-MSi<sub>3</sub>As<sub>3</sub> building blocks. <sup>17,23</sup> The presence of direct covalent Tt-Pn bonding between these local units stabilizes the overall NCS crystal structure. When considering transition metal phosphides or silicides, the regular occurrence of a NCS structure is ~15% statistically; however a vast majority (95%) of ternary M-Si-P crystal structures are NCS for compositions with  $M/(Si+P) < 1.^{28}$  For M-Si-P with  $fac-MSi_3P_3$  building blocks, the strong ligand field nature of Si resulted in low spin electron configuration for transition metals. In turn, this leads to the formation of semiconducting phases for  $d^6$  low-spin electronic configurations, such as  $Ru^{2+}$  or  $Ir^{3+}.^{16}$  We have shown that  $RuSi_4P_4$  and  $IrSi_3P_3$  exhibit an outstanding combination of SHG and LDT despite both materials lacking phase matching properties. Moreover, Ru and Ir are scarce and expensive metals. In this work, we developed cheaper and more earth-abundant alternative IR-NLO materials, FeSi<sub>4</sub>P<sub>4</sub> and CoSi<sub>3</sub>P<sub>3</sub>. Both materials show phase-matchable properties with a 2.09 µm laser and ~3.0 times for CoSi<sub>3</sub>P<sub>3</sub> and ~2.5 times for FeSi<sub>4</sub>P<sub>4</sub> better SHG performance for the largest studied particle size and >2 times increase LDT with a 1.09 µm laser and a pulse width of 10 ns as compared to state-of-the-art AgGaS<sub>2</sub>. In addition, the growth of millimeter-sized single crystals of the Fe- and Co-containing phases have been demonstrated herein. FeSi<sub>4</sub>P<sub>4</sub> and CoSi<sub>3</sub>P<sub>3</sub> are stable in acidic environment and when heated in air to at least 800°C. The cost of the components is another advantage of the developed materials. The prices of the components to make 1 kg of NLO material based on current element market price are: FeSi<sub>4</sub>P<sub>4</sub> (\$1.87), CoSi<sub>3</sub>P<sub>3</sub> (\$9.86), LiInSe<sub>2</sub> (\$82.7), and AgGaS<sub>2</sub> (\$275.2).<sup>29</sup> Therefore, materials for LiInSe<sub>2</sub> and AgGaS<sub>2</sub> are approximately 50-150 times more expensive than FeSi<sub>4</sub>P<sub>4</sub>.

#### **Results and Discussion**

The original reported synthesis for FeSi<sub>4</sub>P<sub>4</sub> and CoSi<sub>3</sub>P<sub>3</sub> included a direct reaction from elements with subsequent grindings and long annealing periods to isolate bulk powder samples.<sup>30,31</sup> In

addition, crystal growth using Sn flux was reported. Cooling of the reaction mixture from 1127 °C to 777 °C at a rate of 1 °C/h (350h long) was reported to produce ~0.2 mm diameter crystals.<sup>30</sup> A recent report by Yu *et al.*, demonstrated the optimization of flux growth synthesis for FeSi<sub>4</sub>P<sub>4</sub> which resulted in the isolation of ~3 mm crystals using Sn flux and stoichiometric amounts of the respective elements.<sup>32</sup> However, there were no details of the synthetic optimization for the isolation of phase pure bulk polycrystalline samples.

Our synthetic methods utilize arc-melted metal silicide precursors to obtain phase-pure samples.  $^{16,20,33,34}$  This procedure guarantees atomic mixing of the refractory constituents (M and Si), making the formation of binary M or Si phosphide admixtures less favorable. This is a new synthetic route for title materials, but similar approached have been applied to prepare complex intermetallics.  $^{35-39}$  FeSi<sub>4</sub>P<sub>4</sub> and CoSi<sub>3</sub>P<sub>3</sub> bulk powder samples were synthesized by stoichiometric reaction of a metal silicide precursor with elemental phosphorus, i.e. FeSi<sub>4</sub> + 4P or CoSi<sub>3</sub> + 3P. The reactants were ground together and heated over 14 h to 1050 °C, annealed for 72 h and then cooled to room temperature by turning off the furnace. This new synthetic route resulted in a significant reduction in reaction time from 2 weeks to 3 days and yielded a single-phase polycrystalline sample of FeSi<sub>4</sub>P<sub>4</sub> (**Figure S1**) and a sample with majority phase being CoSi<sub>3</sub>P<sub>3</sub> (**Figure S2**). Single crystals were grown using the arc-melted precursor, phosphorus powder, and Sn flux. The

reaction products after molten Sn centrifugation were washed in a 1:1 HCl solution. On average 2×2×1 mm<sup>3</sup> and 1×1×1 mm<sup>3</sup> sized crystals of FeSi<sub>4</sub>P<sub>4</sub> and CoSi<sub>3</sub>P<sub>3</sub> were isolated, respectively (**Figures S1 and S2 insets**). We found it necessary to go to higher temperatures and then slow cool to enhance crystal growth, which was previously utilized by Yu *et al.*<sup>32</sup> Since CoSi<sub>3</sub>P<sub>3</sub> powder could not be produced in phase pure form, property measurements were conducted by hand-selected single crystals, which were ground into powders for further characterizations. Both materials were characterized with solid state NMR (ssNMR) and Infrared (FTIR) spectroscopies, powder X-ray diffraction (PXRD), single-crystal X-ray diffraction (SCXRD), energy dispersive X-ray spectroscopy (EDS), thermogravimetric analysis and differential scanning calorimetry (TGA/DSC), computations, diffuse reflectance spectroscopy, and NLO properties measurements (see Supporting Information for methods details).

FeSi<sub>4</sub>P<sub>4</sub> and CoSi<sub>3</sub>P<sub>3</sub> are acid and air stable after a couple of days and after 6 months exposure to 1:1 HCl:H<sub>2</sub>O and air, respectively. Differential scanning calorimetry (DSC) measurements in evacuated and sealed silica ampoules show both stated compounds are thermally stable up to

1100°C (**Figures S3a, S3b, S4a, S4b**). Both materials also have remarkable air-stability at elevated temperatures. Thermal gravimetric analysis/differential scanning calorimetry (TGA/DSC) experiments in air reveal that FeSi<sub>4</sub>P<sub>4</sub> is stable up to 900 °C. Thereafter, there is an inflection in the sample weight followed by an exponential increase up to 160 wt.-% (**Figure S17a**). The weight gain is complemented by the exothermic peak observed in the DSC (**Figure S17a**) which may indicate oxidation of the material, which was confirmed by PXRD analysis of sample after TGA experiment (**Figure S17b**). CoSi<sub>3</sub>P<sub>3</sub> exhibits no substantial weight change to 800 °C and then a moderate increase in weight upon further heating, but no visible peaks the DSC (**Figure S17a**). PXRD shows CoSi<sub>3</sub>P<sub>3</sub> remains unchanged after heating in air to 1100°C (**Figure S17b**). Therefore, we can state that both materials are stable against high temperature air treatment, and that CoSi<sub>3</sub>P<sub>3</sub> is more stable than FeSi<sub>4</sub>P<sub>4</sub>.

FeSi<sub>4</sub>P<sub>4</sub> was reported to crystallize in the noncentrosymmetric space group P1 (No. 1), with 1 Fe, 4 Si, and 4 P sites.<sup>30</sup> Our crystal structure solution agrees with the previously reported structure with  $R_1$  value of 0.022 and a Flack parameter value of 0.012(7) (**Table S1**). In the crystal structure of FeSi<sub>4</sub>P<sub>4</sub> fac-[FeSi<sub>3</sub>P<sub>3</sub>] octahedral units occupy corners of the unit cell (Figure 1a and 1b). The octahedral units are connected via staggered ethane-like [P<sub>3</sub>-Si-P-Si<sub>3</sub>] units, composed of SiP<sub>4</sub> and PSi<sub>4</sub> tetrahedra sharing one Si-P bond between their centra. The P and Si atoms surrounding the central atom form the vertices of the fac-[FeSi<sub>3</sub>P<sub>3</sub>] octahedra, forming Si-Fe and P-Fe bonds. Within the Si-P network, the layers of interconnected Si-P chains are stacked along [100]. These Si-P layers have voids where the Fe atoms reside (Figure 1c). EDS analysis confirms the composition of the Fe compound to be FeSi<sub>3,93(8)</sub>P<sub>4,39(6)</sub> averaged over several sites on different crystallites (Figure S5). The small overestimation of light element P is common for transition metal phosphides. The stability of the structure can be explained using the Zintl-Klemm counting scheme, assuming the ionic nature of Fe-Si and Fe-P interactions. One Si atom forms four covalent bonds to P, thus being Si<sup>0</sup>, and three Si atoms forms three covalent bonds to P, thus being Si<sup>1-</sup> each. In addition, one P atom is bonded to four Si atoms, thus being P<sup>1+</sup>, and three P atoms form three bonds to Si, thus being P<sup>0</sup> each. This leads to a 2+ oxidation state for iron, yielding an electronic-balanced and semiconducting composition:  $(Fe^{2+})(Si^0)(Si^{1-})_3(P^0)_3(P^{1+})$ . Si is a strong field ligand, thus a low-spin closed-shell  $d^6$  configuration for Fe is expected.

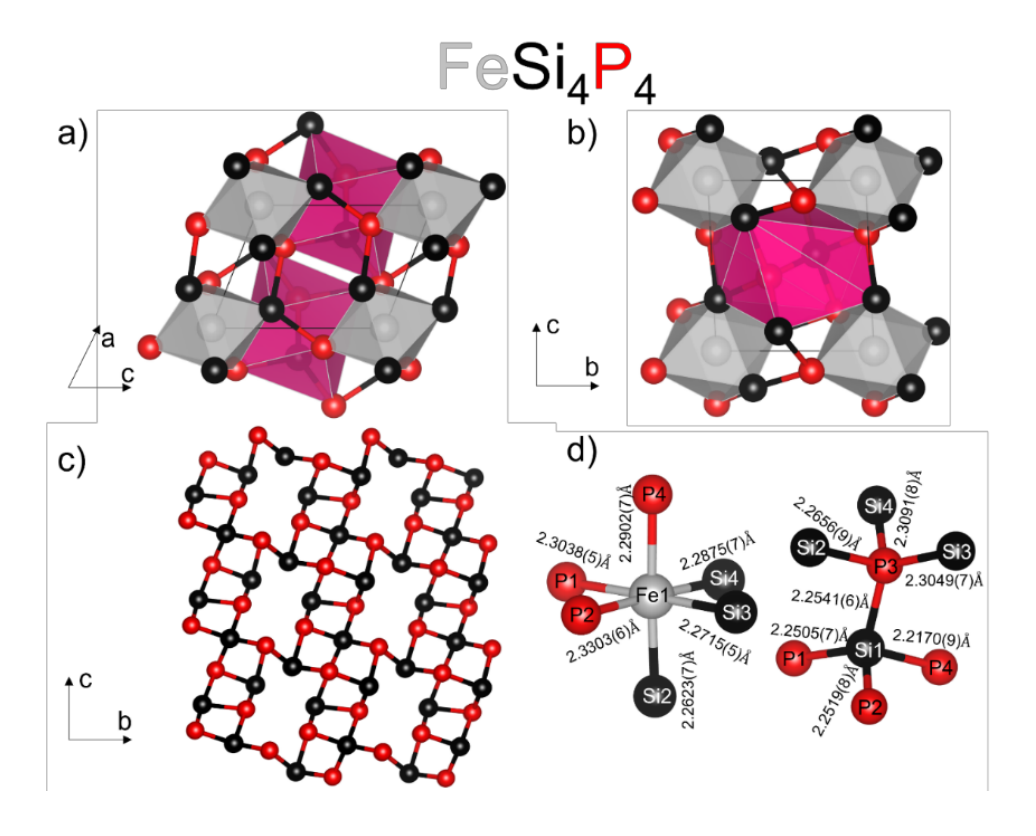


**Figure 1.** Crystal structure of FeSi<sub>4</sub>P<sub>4</sub> (Fe: grey, Si: black, P: red). The unit cell is outlined in black. a), b) General views showing *fac*-[FeSi<sub>3</sub>P<sub>3</sub>] octahedra (grey) and [-P<sub>3</sub>-Si-P-Si<sub>3</sub>-] trigonal antiprisms (dark pink). c) Si-P network with Fe atoms omitted for clarity. d) Isolated octahedral unit of *fac*-[FeSi<sub>3</sub>P<sub>3</sub>] and trigonal antiprism units of [-P<sub>3</sub>-Si-P-Si<sub>3</sub>-] with interatomic distances.

CoSi<sub>3</sub>P<sub>3</sub> was originally reported to crystallize in monoclinic noncentrosymmetric chiral and polar space group,  $P2_1$  (No. 4) with the acknowledgement of a possibility to refine the crystal structure in the orthorhombic chiral and non-polar space groups  $P2_12_12_1$  (No. 19).<sup>31</sup> The subtle difference between the two models lies in the assignment of P and Si sites, which have similar X-ray scattering factors. After refinement, the authors concluded the crystal structure to be monoclinic  $P2_1$  with 2 Co, 6 Si, and 6 P sites.<sup>31</sup> Initial refinements of our own data showed that CoSi<sub>3</sub>P<sub>3</sub> could be solved in both space groups stated above. However, the refined  $\beta$  angle was clearly different from 90 degrees being 90.125(2)°. We refined crystal structure in  $P2_1$ , which resulted in an  $R_1$  value of 0.031 and a Flack parameter value of 0.035(7) (**Table S1**). The crystal structure of CoSi<sub>3</sub>P<sub>3</sub> is composed of the *fac*-[CoSi<sub>3</sub>P<sub>3</sub>] distorted octahedra, [SiP<sub>4</sub>] tetrahedra occupying the corners of the unit cell, and [PSi<sub>4</sub>] tetrahedra occupying the center of the unit cell (**Figure 2a** and **2b**). Unlike in the structure of FeSi<sub>4</sub>P<sub>4</sub>, the SiP<sub>4</sub> and PSi<sub>4</sub> tetrahedra do not overlap and they share two corners

with tetrahedra of the same kind forming one-dimensional  $_{\infty}^{1}[SiP_{2}P_{2/2}]$  and  $_{\infty}^{1}[PSi_{2}Si_{2/2}]$  chains running along [010] direction (**Figure 2c**).

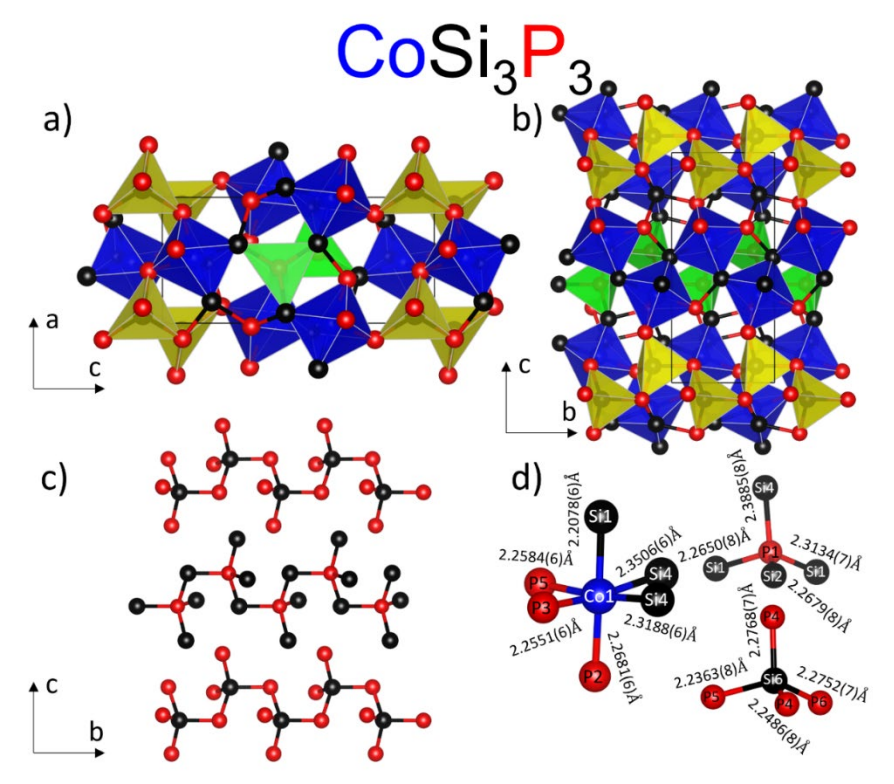


**Figure 2.** Crystal structure of CoSi<sub>3</sub>P<sub>3</sub> (Co: blue, Si: black, P: red). The unit cell is outlined in black. a), b) General views with *fac*-[CoSi<sub>3</sub>P<sub>3</sub>] octahedra shown in blue, [SiP<sub>4</sub>] tetrahedra shown in yellow, and [PSi<sub>4</sub>] tetrahedra in green. c) Si-P network with Co atoms omitted for clarity. d) Isolated octahedral *fac*-[CoSi<sub>3</sub>P<sub>3</sub>] and tetrahedral [SiP<sub>4</sub>] and [PSi<sub>4</sub>] units with interatomic distances.

EDS confirmed the composition to be  $CoSi_{2.83(3)}P_{3.14(6)}$  averaged over several sites on different crystals (**Figure S6**). Zintl-Klemm formalism can be applied as followed: one Si atom forming four covalent bonds to P (Si<sup>0</sup>), another Si atom forming two bonds to P (Si<sup>2-</sup>), and four Si atoms forming three Si-P bonds (Si<sup>1-</sup>); one P atom forming four bonds to Si assigned as P<sup>1+</sup>, another P atom forming two bonds to Si (P<sup>1-</sup>), and four P atom forming three bonds to Si (P<sup>0</sup>). Thereby, an electron-balanced formula can be written as  $(Co^{3+})_2(Si^0)(Si^{2-})(Si^{1-})_4(P^{1+})(P^{1-})(P^0)_4$ . Low-spin Co<sup>3+</sup> is expected to have closed-shell  $d^6$  electronic configuration.

FeSi<sub>4</sub>P<sub>4</sub> and CoSi<sub>3</sub>P<sub>3</sub> contain transition metals and main group elements which have a small difference of electronegativities. The Pauling electronegativities<sup>40</sup> of Fe (1.8), Co (1.9), Si (1.9), and P (2.2) are comparable which give the metal the ability to form covalent bonds with Si and P.

In the crystal structure of FeSi<sub>4</sub>P<sub>4</sub>, the Fe-Si distances (2.26-2.29 Å) are shorter than the Fe-P ones (2.29-2.33 Å) (Table S2). This is unexpected based on the covalent radii trend, because Si (1.17 Å) is larger than P (1.11 Å). The observed difference can be explained assuming that  $\pi$ -electron backdonation between Fe and Si is more effective than that between Fe and P. A similar M-Si distance shortening was observed in other metal silicon phosphides. <sup>16,24</sup> For CoSi<sub>3</sub>P<sub>3</sub> larger ranges for distances were observed, Co-Si (2.20-2.35 Å) and Co-P (2.23-2.32 Å) (Table S2), yet the average Co-Si and Co-P distances are close (2.27 Å) in contradiction with the covalent radii trend. Following the original discussion, the crystal structure of the CoSi<sub>3</sub>P<sub>3</sub> was also refined in the orthorhombic P2<sub>1</sub>2<sub>1</sub>2<sub>1</sub> space group mentioned by Perrier, et al.<sup>31</sup> In this case, the structure displayed mer-[CoSi<sub>3</sub>P<sub>3</sub>] octahedral units and [Si@SiP<sub>3</sub>] and [P@PSi<sub>3</sub>] tetrahedral units (Figure S7), neither of which were observed in other transition metal silicon phosphides. All reported transition metal silicon phosphides show no homoatomic Si-Si or P-P bonding, while such homoatomic bonds are common in alkaline-earth and rare-earth silicon-phosphides. 15,20,24,41-45 Solid-state NMR (ssNMR) was further applied to corroborate the two structural models derived from X-ray diffraction. SCXRD is a dominant technique for the characterization of long-range ordering in solids. In SCXRD there is a prominent reliance on chemical knowledge to identify elements with similar scattering factors, such as Si and P, which may lead to incorrect structural models.16,46

<sup>31</sup>P and <sup>29</sup>Si ssNMR spectroscopy was used to characterize both FeSi<sub>4</sub>P<sub>4</sub> and CoSi<sub>3</sub>P<sub>3</sub> (**Figure 3a** and **3b**). The SCXRD model for FeSi<sub>4</sub>P<sub>4</sub> shows four unique crystallographic sites for Si and P atoms. Therefore, we expect to see at most four unique peaks in each of the <sup>31</sup>P and <sup>29</sup>Si ssNMR spectra. The <sup>31</sup>P ssNMR spectrum of FeSi<sub>4</sub>P<sub>4</sub> unambiguously shows there are four peaks with an isotropic chemical shift of –26.3, –75.0, –95.0, and –127.8 ppm (**Figure 3a**). The <sup>29</sup>Si ssNMR spectrum shows three resolved peaks with chemical shifts of 53.9, 19.0, and –23.9 ppm. Fitting the <sup>29</sup>Si NMR spectrum results in a 1:2:1 integrated intensity ratio for the 3 peaks (**Figure 3b**, **Table S3**). Therefore, the <sup>29</sup>Si NMR spectrum is also composed of four peaks with two of them overlapping due to similar chemical shifts. To improve the sensitivity of <sup>29</sup>Si NMR experiments we used the Carr-Purcell-Meiboom-Gill (CPMG) pulse sequence. CPMG acquisition provides a significant boost in signal-to-noise ratio as compared to a spin echo spectrum (**Figure S8**). While CPMG is a non-qualitative technique, we find that peak intensities in the CPMG spectrum and a spin echo spectrum closely matched (**Table S4**). <sup>31</sup>P and <sup>29</sup>Si chemical shift ranges for FeSi<sub>4</sub>P<sub>4</sub> are

similar to other semiconducting transition metal silicon phosphide phases of isostructural RuSi<sub>4</sub>P<sub>4</sub> (space group P1) and IrSi<sub>3</sub>P<sub>3</sub> (space group Cm).

The previously reported chemical shift for RuSi<sub>4</sub>P<sub>4</sub> was -70.6, -93.1, -121.4, and -135.5 ppm (31P) and 52.8, 39.2, 28.1, and -12.3 ppm (<sup>29</sup>Si). The IrSi<sub>3</sub>P<sub>3</sub> chemical shift range is also similar to FeSi<sub>4</sub>P<sub>4</sub>, -160.2 to -184.9 ppm (<sup>31</sup>P) and -1.7 to -29.2 ppm (<sup>29</sup>Si). <sup>16</sup> The analysis of CoSi<sub>3</sub>P<sub>3</sub> required thoughtful consideration of both SCXRD models in the P2<sub>1</sub> and P2<sub>1</sub>2<sub>1</sub>2<sub>1</sub> space groups. In the monoclinic P2<sub>1</sub> model, there are 6 P and 6 Si unique crystallographic sites. In comparison, the orthorhombic P2<sub>1</sub>2<sub>1</sub>2<sub>1</sub> model has only 3 P and 3 Si unique crystallographic sites. The <sup>31</sup>P ssNMR spectrum of CoSi<sub>3</sub>P<sub>3</sub> exhibits at least eight distinguishable peaks with chemical shifts ranging from 200 ppm to -150 ppm (**Figure 3c**). We anticipate that the signals between 50 ppm to -150pm in the <sup>31</sup>P NMR spectra corresponds to CoSi<sub>3</sub>P<sub>3</sub> based on the chemical shift range for previously studied transition metal silicon phosphides. 47-49 The peaks outside this range are attributed to unidentified admixtures. The <sup>29</sup>Si NMR spectrum of CoSi<sub>3</sub>P<sub>3</sub> consists of several broad signals with chemical shifts ranging from 400 ppm to 50 ppm (Figure 3d). The <sup>29</sup>Si NMR spectrum was fitted to six peaks with a chemical shift of 305.2, 268.5, 208.5, 168.2, 142.7, and 94.5 ppm and a consistent 1:1:1:1:1 ratio of the integrated intensities. Although the CoSi<sub>3</sub>P<sub>3</sub> <sup>31</sup>P NMR and <sup>29</sup>Si NMR spectra contain significant peak broadening and show multiple overlapping peaks, they suggest that  $CoSi_3P_3$  crystallizes in the  $P2_1$  space group rather than the alternative  $P2_12_12_1$  space group. The latter model predicts there should be only three unique P signals, which is inconsistent with the observed data. Further NMR investigations are currently in progress to validate this hypothesis and to assign the P NMR signals. Further information on experimental parameters can be found in **Table S5**.

*Perrier* and coworkers utilized Raman spectroscopy to confirm the monoclinic nature of CoSi<sub>3</sub>P<sub>3</sub> with multiple bands observed in the 100-550 cm<sup>-1</sup> frequency range.<sup>31</sup> Raman studies of FeSi<sub>4</sub>P<sub>4</sub> also indicated that most of the framework Fe-Si-P vibrations occur in 100-550 cm<sup>-1</sup> range.<sup>32</sup> We performed FTIR characterization of both materials in the accessible spectrometer range of 400-4000 cm<sup>-1</sup> (**Figure S18a**). In the 400-550 cm<sup>-1</sup> frequency range the observed FTIR spectra qualitatively agrees with the reported Raman spectra (**Figure S18b**) (note that for *P*1 and *P*2<sub>1</sub> all vibrational bands are Raman and IR active).

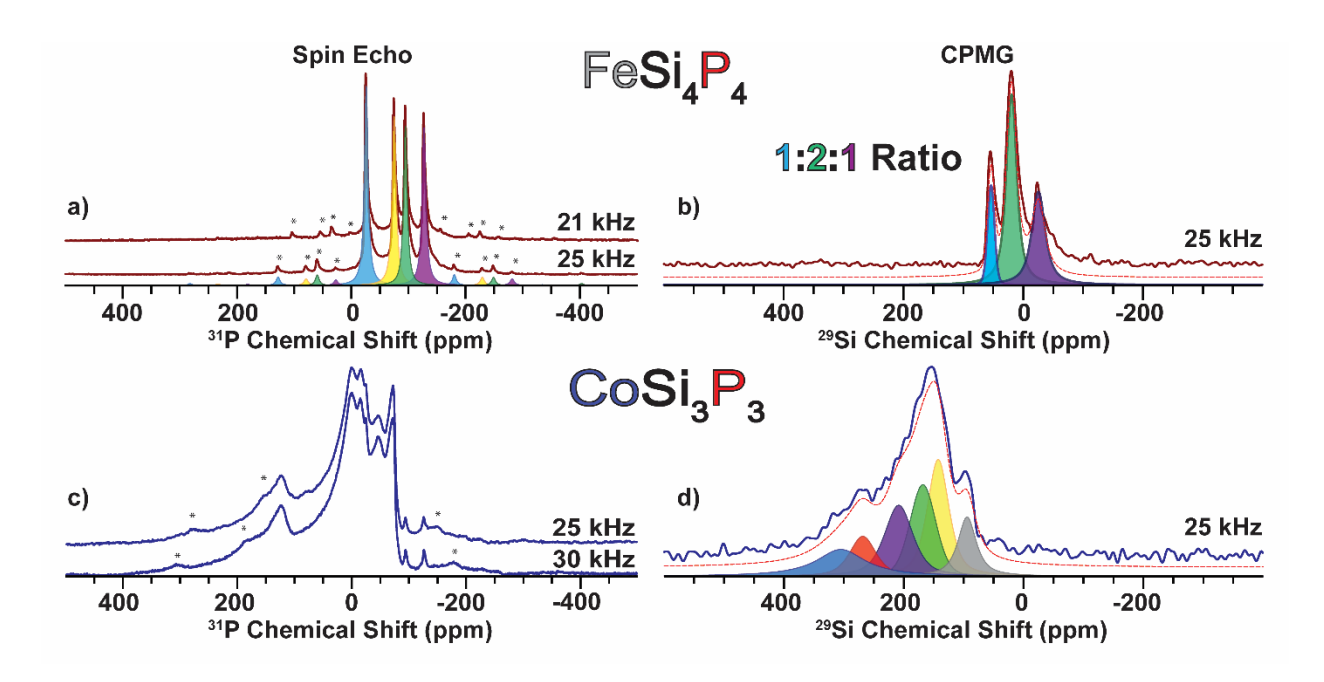


**Figure 3.** a), c) Direct excitation of <sup>31</sup>P and b), d) <sup>29</sup>Si MAS ssNMR spectra of a), b) FeSi<sub>4</sub>P<sub>4</sub> and c), d) CoSi<sub>3</sub>P<sub>3</sub>. The MAS frequency used for acquisition of the spectra is indicated. Asterisks (\*) denote spinning sideband signals.

The proposed from Zintl-Klemm formalism charge-balanced semiconducting nature of the studied materials was confirmed with electronic structure calculations (*vide infra*) and experimental optical measurements. The UV-Vis measurements showed that FeSi<sub>4</sub>P<sub>4</sub> and CoSi<sub>3</sub>P<sub>3</sub> are indirect bandgap semiconductors. From the analysis of Tauc plots the indirect and direct bandgaps were estimated (**Table 1**, **Figure 4a**, **Figure S9**). The direct bandgaps of 1.3 eV (FeSi<sub>4</sub>P<sub>4</sub>) and 1.6 eV (CoSi<sub>3</sub>P<sub>3</sub>) are consistent with observed black and deep red colors of the corresponding material.

Both materials have NCS structures and relatively narrow bandgaps. The Kurtz and Perry method was utilized for second harmonic generation (SHG) powder measurements for both FeSi<sub>4</sub>P<sub>4</sub> and CoSi<sub>3</sub>P<sub>3</sub> compounds using a *Q*-switch 2.09 μm laser source (3 Hz, 50 ns).<sup>50</sup> The SHG response may be weakened due to their narrow optical bandgap, so reflectance SHG signals were collected. Both materials exhibit strong SHG activity, ~3.0 times for CoSi<sub>3</sub>P<sub>3</sub> and ~2.5 times for FeSi<sub>4</sub>P<sub>4</sub> higher than that of our grown by Bridgman technique AgGaS<sub>2</sub> (AGS) state-of-the-art standard in the 207-257 μm particles sizes range (**Figure 4b, Table S6**).

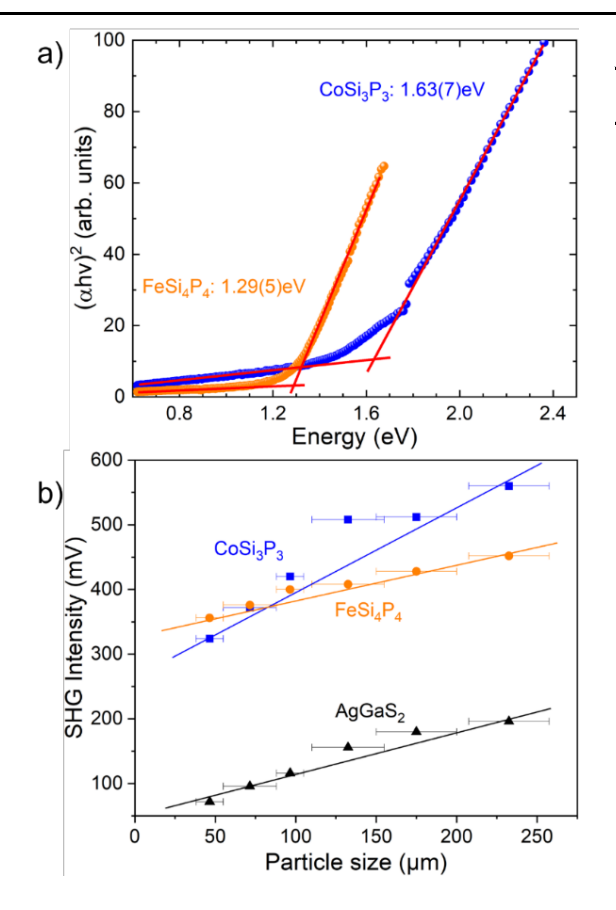


| Table 1. | Experimental | and | calculated | bandgaps | (eV). |
|----------|--------------|-----|------------|----------|-------|
|          |              |     |            |          |       |

| Compound         | FeSi <sub>4</sub> P <sub>4</sub> |          | CoSi <sub>3</sub> P <sub>3</sub> |          |  |
|------------------|----------------------------------|----------|----------------------------------|----------|--|
| Bandgap          | Direct                           | Indirect | Direct                           | Indirect |  |
| Experimental     | 1.29(5)                          | 1.18(5)  | 1.63(5)                          | 1.46(5)  |  |
| Calculated (LDA) | 1.26                             | 0.96     | 1.36                             | 1.23     |  |
| Calculated (HSE) | 2.10                             | 1.80     | 2.05                             | 1.90     |  |

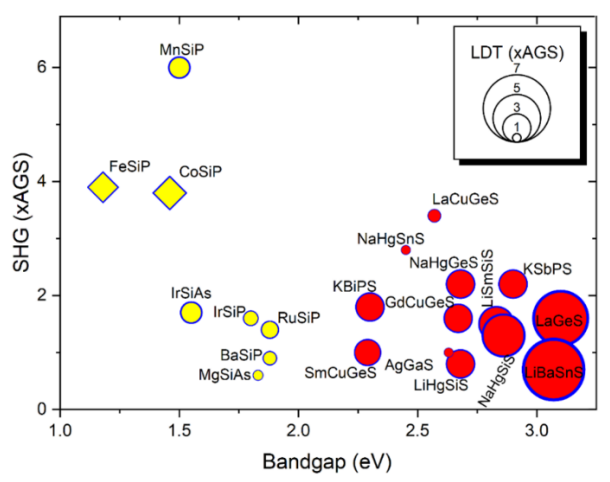


**Figure 4.** a) Direct bandgap Tauc plots for FeSi<sub>4</sub>P<sub>4</sub> and CoSi<sub>3</sub>P<sub>3</sub>. b) Second harmonic generation of FeSi<sub>4</sub>P<sub>4</sub>, CoSi<sub>3</sub>P<sub>3</sub>, and AgGaS<sub>2</sub> powders measured in identical conditions at various particle sizes.

Figure 5. Diagram showing the dependence of SHG signal (vertical scale) to bandgap (horizontal scale) with LDT (symbol diameter). FeSi<sub>4</sub>P<sub>4</sub>, CoSi<sub>3</sub>P<sub>3</sub>, and metal silicon phosphides materials are labeled in yellow symbols. AgGaS<sub>2</sub> and other selected chalcogenide materials are labeled in red symbols. Expansions for abbreviations can be found in Table S6.

FeSi<sub>4</sub>P<sub>4</sub> and CoSi<sub>3</sub>P<sub>3</sub> performance in the 54-88  $\mu$ m particles sizes range is better than most ternary silicon pnictides such as IrSi<sub>3</sub>P<sub>3</sub> (1.6× AGS), <sup>16</sup> IrSi<sub>3</sub>As<sub>3</sub> (1.7× AGS), <sup>17</sup> RuSi<sub>4</sub>P<sub>4</sub> (1.4× AGS), <sup>16</sup> MgSiAs<sub>2</sub> (0.6× AGS), <sup>14</sup> and Ba<sub>2</sub>Si<sub>3</sub>P<sub>6</sub> (0.9× AGS)<sup>15</sup> (**Figure S10**, **Table S6**). The only silicon phosphide with higher SHG signal is MnSiP<sub>2</sub> (6× AGS), but MnSiP<sub>2</sub> was measured at different

excitation wavelength.<sup>13</sup> All previously reported silicon-phosphide materials were not phase-matchable, which prevents their practical application as NLO materials. In turn, FeSi<sub>4</sub>P<sub>4</sub> and CoSi<sub>3</sub>P<sub>3</sub> demonstrated a linear increase of SHG response with particle size, i.e., phase-matching, which further makes them attractive for practical applications. In addition, these materials have strong SHG responses, which outperform the majority of chalcogenide NLO materials (**Figure 5**).

First-principles calculations were used to investigate the optical properties of both FeSi<sub>4</sub>P<sub>4</sub> and CoSi<sub>3</sub>P<sub>3</sub> in the framework of density-functional theory (DFT) and density-functional pertrubation theory (DFPT).<sup>51</sup> The exchange-correlation energy was modeled with the local-density approximation (LDA).<sup>52</sup> The relaxation of the crystal structure yielded cell parameters within 2% of the experimental ones, following the usual underestimation inherent to LDA functionals. More details on the computations can be found in the Supporting Information. The calculated electronic band structures are reported in Figure 6. As proposed in the structural analysis discussion, the covalency of M-Si and M-P interactions manifests in good mixing of M-3d states with P-3p and Si-3p states in the band structures of studied compounds. The corresponding bandgaps can be found in Table 1. The excellent agreement of the direct bandgaps with their experimental counterpart is quite surprising. Usually, local or semi-local functionals tend to severely underestimate the experimental value. For both compounds, the fundamental gap is indirect which agrees with the experiment. When adopting the Heyd-Scuseria-Ernzerhof (HSE) exchangecorrelation functional,<sup>53</sup> the calculated fundamental gap remained indirect but the incidental agreement of the direct gaps with the experiment was lost, as shown in Table 1. The direct bandgap of both materials heavily influences their optical properties. Thereby, we decided to keep the calculated LDA bandgaps for the subsequent calculations.

The nonlinear optical properties were then investigated. The static high-frequency SHG tensor  $d_{ij}^{\infty}$  was computed using DFPT and, for FeSi<sub>4</sub>P<sub>4</sub>, it yielded:

$$d_{ij}^{\infty} = \begin{bmatrix} 24.26 & -6.13 & 9.00 & 7.11 & 18.38 & 15.85 \\ 15.85 & 54.82 & 19.49 & 17.27 & 7.11 & -6.13 \\ 18.38 & 17.27 & 27.96 & 19.49 & 9.00 & 7.11 \end{bmatrix}$$

while, for CoSi<sub>3</sub>P<sub>3</sub>, it was:

$$d_{ij}^{\infty} = \begin{bmatrix} 0 & 0 & 0 & -33.44 & 0 & 3.76 \\ 3.76 & -92.62 & 3.82 & 0 & -33.44 & 0 \\ 0 & 0 & 0 & 3.82 & 0 & -33.44 \end{bmatrix}$$

Equation 1 demonstrates that the ratio of the experimental SHG intensities, I, can be linked to a ratio of effective coefficients,  $d_{eff}$ , derived from the tensors and the superscript (R) indicates the reference sample.  $^{50,54}$ 

$$\left(\frac{d_{eff}}{d_{eff}^{(R)}}\right)^2 = \frac{I}{I^{(R)}},\tag{Eq. 1}$$

It was decided to use the root mean square of the SHG components as an effective coefficient. This value constitutes an invariant of third-rank tensors while embodying the averaging concept of the powder technique. SA a result, FeSi4P4 and CoSi3P3 possess an effective coefficient of 18.09 pm/V and 23.86 pm/V, respectively. The only non-zero component of AgGaS2,  $d_{36}$ , can vary quite drastically in the literature. For this reason, the DFPT SHG tensor of AgGaS2 was also computed in this work following the same procedure as for FeSi4P4 and CoSi3P3, except that a scissor of 1.7 eV was applied to match the experimental bandgap of 2.64 eV. Using the ratio of effective coefficients, we can calculate the different SHG values between our reference, AgGaS2, and the studied ternary tetrel pnictides (**Table S7**). In practice, a ratio of intensities of 4 is equivalent to an effective coefficient in-between 6.6 pm/V and 32.8 pm/V for FeSi4P4 and CoSi3P3, which is in line with the DFPT results.

The frequency-dependent  $d_{22}$ , the largest component of the SHG tensor, was also computed (see **Figure S11** and **S12**). A band-resolved analysis was further performed to understand the origin of the SHG response for the two compounds at hand.<sup>57</sup> The total frequency-dependent SHG response is the sum of two- or three-band contributions. In a band-resolved analysis, the latter are isolated and then partially summed over, such that the total contribution of each individual valence and conduction band is recovered. This allows one to quantify the contribution of each band to the SHG response at a given frequency as illustrated in **Figure 6**. The investigated frequency was chosen based on the following sum rule,

$$\Re(\chi^{(2)}(0,0,0)) = \frac{2}{\pi} P \int \frac{\Im(\chi^{(2)}(-2\omega,\omega,\omega))}{\omega} d\omega,$$

which dictates that the magnitude of the static real part of a coefficient is directly related to the main peak of its imaginary spectrum. It is thus interesting to perform the band-resolved analysis of this peak to understand  $\chi^{(2)}(0,0,0)$ . As can be seen in **Figures S13** and **S14**, this peak is located at 1.06 eV and 0.87 eV for FeSi<sub>4</sub>P<sub>4</sub> and CoSi<sub>3</sub>P<sub>3</sub>, respectively. The "Intra 2 $\omega$ " and "Inter 2 $\omega$ " denominations refer to the 2 $\omega$ -resonant intra- and interband transitions, respectively. Together with the "IntraS" term, i.e., the modulation of the interband terms by intraband ones, and their 1 $\omega$ -resonant counterpart, they constitute the total SHG response as introduced by Sipe and Ghahramani. The origin of these three terms lies in the mathematical development of the Hamiltonian when deriving the sum-over-states equation.

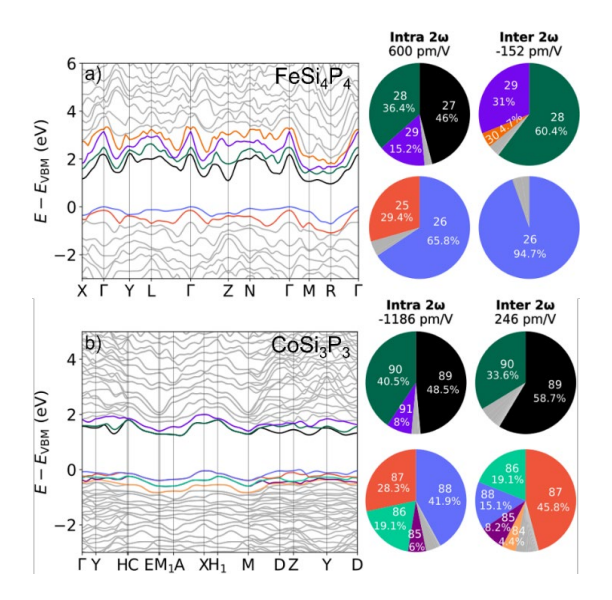


**Figure 6.** a) Band-resolved analysis of the imaginary part of the  $d_{22}$  coefficient of FeSi<sub>4</sub>P<sub>4</sub> at 1.06 eV. b) Band-resolved analysis of the imaginary part of the  $d_{22}$  coefficient of CoSi<sub>3</sub>P<sub>3</sub> at 0.87 eV. The electronic structure bands are color-coded (left) to relate with the pie charts (right), which are associated with the individual contributions of the most important bands to the SHG response. Only the three-bands interactions were considered as the two-bands ones are negligible. The bands are shifted to set the valence band maximum (VBM) at 0 eV.

To the best of our knowledge, a clear physical interpretation of those terms is still lacking. Fortunately, it is not required in the context of the present band-resolved analysis. In line with the expectations, the first bands on both sides of the gap are the major contributor to the SHG response, which is expected (**Figure 6**). To complement this analysis, a projected density of states (PDOS) was computed (**Figure S15** and **S16**). In FeSi<sub>4</sub>P<sub>4</sub>, the SHG response mainly comes from Fe-3*d*, Si-

3*p*, and P-3*p* contributions. Similarly, in CoSi<sub>3</sub>P<sub>3</sub>, the orbitals Co-3*d*, Si-3*p*, and P-3*p* are mainly responsible for the SHG. Our computational exploration supports the experimentally observed linear and non-linear optical properties of FeSi<sub>4</sub>P<sub>4</sub> and CoSi<sub>3</sub>P<sub>3</sub> as well as the hypothesis regarding strong covalent bonding interactions between transition metal, silicon, and phosphorus.

Besides phase-matchability and SHG intensity, the laser damage threshold (LDT) is an important characteristic of NLO material. LDT measurements are less standardized than SHG ones and different values of LDT were reported for the powders of AGS standard, ranging from 1 to 30 MW cm<sup>-2</sup> even for the same laser wavelength 1.06 µm. The different pulse sequences and varying quality of AGS standard may be responsible for the large discrepancy of the LDT reports for AGS. Nevertheless, single crystals of AGS were reported to have LDT of ~30 MW cm<sup>-2</sup>. To avoid comparing apples to oranges, we limited the following discussion to such examples of reported LDTs where measurements of AGS LDT at the same setup and identical conditions generated LDT of 28-32 MW cm<sup>-2</sup>. Generally, chalcogenides materials have an established trend of a positive relationship between bandgap and LDT, i.e., small bandgap materials show high SHG activity but low LDT and vice versa. For example, Li<sub>2</sub>BaSnS<sub>4</sub> has a 3.07 eV bandgap exhibits a low SHG intensity (0.7× AGS) but a high LDT value (192 MW cm<sup>-2</sup>)<sup>60</sup> (Figure 5, 7, and S10). The LDT values for FeSi<sub>4</sub>P<sub>4</sub> (68 MW cm<sup>-2</sup>, 2.3× AGS) and CoSi<sub>3</sub>P<sub>3</sub> (74 MW cm<sup>-2</sup>, 2.5× AGS) are particularly exceptional for small bandgap semiconductors (Table S6). Due to strong covalent M-P and M-Si bonds, transition metal silicon phosphides exhibit higher LDT values, such as MnSiP<sub>2</sub> (70 MW cm<sup>-2</sup>), <sup>13</sup> IrSi<sub>3</sub>P<sub>3</sub> (48 MW cm<sup>-2</sup>), <sup>16</sup> IrSi<sub>3</sub>As<sub>3</sub> (68 MW cm<sup>-2</sup>), <sup>17</sup> and RuSi<sub>4</sub>P<sub>4</sub> (58 MW cm<sup>-2</sup>) <sup>2</sup>), <sup>16</sup> than alkaline-earth silicon phosphides, MgSiAs<sub>2</sub> (33 MW cm<sup>-2</sup>), <sup>14</sup> and Ba<sub>2</sub>Si<sub>3</sub>P<sub>6</sub> (45 MW cm<sup>-2</sup>) <sup>2</sup>)<sup>18</sup> (Figure 7, Table S6, Figure S10). Transition metal silicon-phosphides break the trend observed in chalcogenide materials by showing consistent LDT even for materials with small bandgaps, < 2 eV. Confirmed by our calculational evaluations, the strong covalency of {Co,Fe}-{Si,P} bonds contributes to the high LDT of the studied compounds. We hypothesized that the higher ionic component of M-S and M-Se bonding makes chalcogenides more susceptible to laser irradiation and higher bandgap are required for chalcogenides to achieve high LDT.

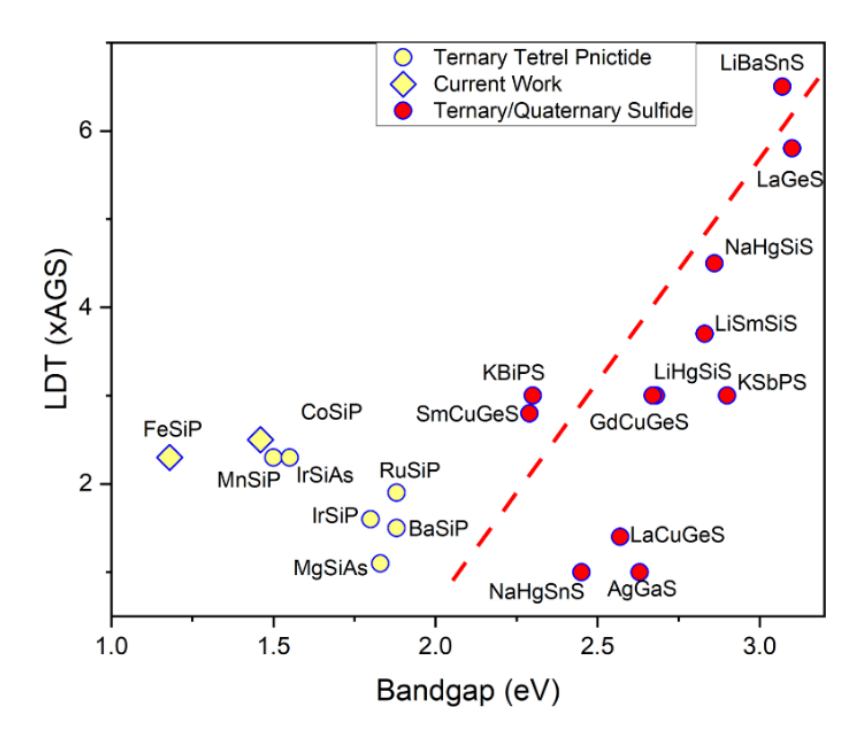


**Figure 7.** Band gap dependence of the normalized LDT values for ternary phosphides (labeled in yellow) and selected ternary/quaternary sulfides (labeled in red) that were experimentally verified to be phase-matching materials. Expansions for abbreviations can be found in **Table S6**.

# **Conclusions**

We developed a synthetic approach to produce powdered samples and millimeter-sized crystals of FeSi<sub>4</sub>P<sub>4</sub> and CoSi<sub>3</sub>P<sub>3</sub>. The crystal structures of these NCS moderate bandgap semiconductors were redetermined through SCXRD and <sup>29</sup>Si, <sup>31</sup>P MAS NMR techniques. FeSi<sub>4</sub>P<sub>4</sub> is confirmed to crystallize in *P*1 space group, while CoSi<sub>3</sub>P<sub>3</sub> is confirmed to crystallize in *P*2<sub>1</sub> space group with no homoatomic Si-Si or P-P bonds in either structure. FeSi<sub>4</sub>P<sub>4</sub> and CoSi<sub>3</sub>P<sub>3</sub> demonstrate strong SHG activity and exceptional LDT as compared to the AgGaS<sub>2</sub> state-of-the-art standard. First principles computations confirm the high SHG for these phases and provide their full *d*<sub>ijk</sub> tensor. The calculations attribute the strong NLO response of the title compounds to the covalency of {Fe,Co}-{P-Si} interactions. When comparing to chalcogenide NLO materials, FeSi<sub>4</sub>P<sub>4</sub> and CoSi<sub>3</sub>P<sub>3</sub> are acid stable, have high oxidation resistance, composed of inexpensive and earthabundant elements, and exhibit a healthy balance of SHG response and LDT values with phase-matching.

#### **Author contributions**

K. Kovnir conceived of and supervised the project. E. Soto, S. J. Lee, N. Hewage, G. Akopov conducted the synthesis and majority of experiments. E. Soto organized all the data and wrote the manuscript with K. Kovnir. G. Viswanathan conducted diffuse reflectance experiments. K. Wu conducted nonlinear optical studies. A. P. Porter and A. J. Rossini conducted ssNMR studies. V. Trinquet, G. Brunin, G. Hautier, and G.-M. Rignanese conducted the calculations.

#### **Conflicts of interest**

There are no conflicts to declare.

# **Supporting Information**

The Supporting Information is available free of charge: Experimental and computational methods, and additional figures and tables pertaining to powder X-ray diffraction, scanning electron microscopy/energy dispersive X-ray spectroscopy, ssNMR, TGA/DSC, FTIR, diffuse reflectance spectroscopy, and electronic structure calculations.

# Acknowledgements

We thank Dr. Yaroslav Mudryk (Ames National Laboratory) for access to the arc-melting setup and Professor Julia Zaikina (ISU) for the use of the diffuse-reflectance setup.

# **Funding Sources**

This research was supported by the National Science Foundation under Grant No. 1955456 to K.K. Solid-state NMR spectroscopy experiments (A.P.P. and A.J.R.) were supported by the U.S. Department of Energy (DOE), Office of Science, Basic Energy Sciences, Materials Science and Engineering Division. Ames National Laboratory is operated for the U.S. DOE by Iowa State University under Contract DE-AC02-07CH11358. A.J.R. acknowledges additional support from the Alfred P. Sloan Foundation through a Sloan research fellowship. G.A. is grateful for the support from the Rutgers University, Newark new faculty start-up fund. The theoretical part of the work has been supported in part by the U.S. Department of Energy, Office of Science, Basic Energy Sciences under award number DE-SC0023509. Computational resources have been provided by the supercomputing facilities of the Université catholique de Louvain (CISM/UCL) and the

Consortium des Équipements de Calcul Intensif en Fédération Wallonie Bruxelles (CÉCI) funded by the Fond de la Recherche Scientifique de Belgique (F.R.S.-FNRS) under convention 2.5020.11 and by the Walloon Region. The present research benefited from computational resources made available on Lucia, the Tier-1 supercomputer of the Walloon Region, infrastructure funded by the Walloon Region under grant agreement No. 1910247. V.T. acknowledges the support from the FRS-FNRS through a FRIA Grant.

#### References

- (1) Chu, D.; Huang, Y.; Xie, C.; Tikhonov, E.; Kruglov, I.; Li, G.; Pan, S.; Yang, Z. Unbiased Screening of Novel Infrared Nonlinear Optical Materials with High Thermal Conductivity: Long-neglected Nitrides and Popular Chalcogenides. *Angew. Chem. Int. Ed.* **2023**, *62* (1), e202300581.
- (2) Luo, L.; Wang, L.; Chen, J.; Zhou, J.; Yang, Z.; Pan, S.; Li. J. A<sup>I</sup>B<sub>3</sub><sup>II</sup>C<sub>3</sub><sup>III</sup>Q<sub>8</sub><sup>VI</sup>: A New Family for the Design of Infrared Nonlinear Optical Materials by Coupling Octahedra and Tetrahedra Units. *J. Amer. Chem. Soc.* **2022**, *144* (48), 21916-21925.
- (3) Zhang, H.; Zhang, M.; Pan, S.; Dong, X.; Yang, Z.; Hou, X.; Wang, Z.; Chang, K. B.; Poeppelmeier, K. R. Pb<sub>17</sub>O<sub>8</sub>Cl<sub>18</sub>: A Promising IR Nonlinear Optical Material with Large Laser Damage Threshold Synthesized in an Open System. *J. Am. Chem. Soc.* **2015**, *137* (26), 8360-8363.
- (4) Aslam, H. Z.; Doane, J. T.; Yeung, M. T.; Akopov, G. Advances in Solid-State Nonlinear Optical Materials: From Fundamentals to Applications. *ACS Appl. Opt. Mater.* **2023**, *1* (12), 1898–1921.
- (5) He, J.; Iyer, A. K.; Waters, M. J.; Sarkar, S.; Zu, R.; Rondinelli, J. M.; Kanatzidis, M. G.; Gopalan, V. *Adv. Optical Mater.* **2022**, *10* (2), 2101729.
- (6) Khatun, M.; Stoyko, S. S.; Mar, A. Ternary Arsenides ATt<sub>3</sub>As<sub>3</sub> (A=K, Rb; Tt=Ge, Sn) with Layered Structures. *J. Solid State Chem.* **2016**, *238*, 229–235.
- (7) Weippert, V.; Chau, T.; Witthaut, K.; Johrendt, D. Mixed Valence and Unusual Germanium Coordination in SrGe<sub>8</sub>As<sub>10</sub>, BaGe<sub>8</sub>As<sub>10</sub>, and BaGe<sub>7</sub>P<sub>12</sub>. *Inorg. Chem.* **2020**, *59* (20), 15447–15453.
- (8) Park, Y.; Kanatzidis, M. G. On the Dissolution of Gold in K<sub>2</sub>Q<sub>x</sub> and Na<sub>2</sub>Q<sub>x</sub> Fluxes (Q=S, Se). Formation of KAuS<sub>5</sub>, KAuSe<sub>5</sub>, CsAuSe<sub>3</sub>, KAuSe<sub>2</sub> and NaAuSe<sub>2</sub>: Low-Dimensional Au<sup>+</sup> and Au<sup>3+</sup> Compounds with Poly- and Mono-Chalcogenide Ligands. *J. Alloys Compd.* **1997**, *257*, 137–145.
- (9) Park, Y.; Kanatzidis, M. G. AuCuSe<sub>4</sub>: A Mixed Polychalcogenide with Se<sub>3</sub><sup>2</sup>- and Se<sup>2</sup>- Anions. *Inorg. Chem.* **2001**, *40* (23), 5913–5916.
- (10) Kurzman, J. A.; Ouyang, X.; Im, W. B.; Li, J.; Hu, J.; Scott, S. L.; Seshadri, R. La<sub>4</sub>LiAuO<sub>8</sub> and La<sub>2</sub>BaPdO<sub>5</sub>: Comparing Two Highly Stable d<sup>8</sup> Square-Planar Oxides. *Inorg. Chem.* **2010**, 49 (10), 4670–4680.
- (11) Hahn, H.; Frank, G.; Klingler, W.; Meyer, A.-D.; Störger, G. Untersuchungen über ternäre Chalkogenide. V. Über einige ternäre Chalkogenide mit Chalkopyritstruktur. *Z. anorg. allg. Chem.* **1953**, *271* (3–4), 153–170.
- (12) Harasaki, A. H. A.; Kato, K. K. K. New Data on the Nonlinear Optical Constant, Phase-Matching, and Optical Damage of AgGaS<sub>2</sub>. *Jpn. J. Appl. Phys.* **1997**, *36* (2R), 700.
- (13) Yu, T.; Wang, S.; Zhang, X.; Li, C.; Qiao, J.; Jia, N.; Han, B.; Xia, S.-Q.; Tao, X. MnSiP<sub>2</sub>: A New Mid-IR Ternary Phosphide with Strong SHG Effect and Ultrabroad Transparency Range. *Chem. Mater.* 2019, 31 (6), 2010–2018.
- (14) Woo, K. E.; Wang, J.; Wu, K.; Lee, K.; Dolyniuk, J.-A.; Pan, S.; Kovnir, K. Mg-Si-As: An Unexplored System with Promising Nonlinear Optical Properties. Adv. Funct. Mater. 2018, 28 (30), 1801589.
- (15) Mark, J.; Wang, J.; Wu, K.; Lo, J. G.; Lee, S.; Kovnir, K. Ba<sub>2</sub>Si<sub>3</sub>P6: 1D Nonlinear Optical Material with Thermal Barrier Chains. *J. Am. Chem. Soc.* **2019**, *141* (30), 11976–11983.
- (16) Lee, S.; Carnahan, S. L.; Akopov, G.; Yox, P.; Wang, L.-L.; Rossini, A. J.; Wu, K.; Kovnir, K. Noncentrosymmetric Tetrel Pnictides RuSi<sub>4</sub>P<sub>4</sub> and IrSi<sub>3</sub>P<sub>3</sub>: Nonlinear Optical Materials with Outstanding Laser Damage Threshold. *Adv. Funct. Mater.* **2021**, *31* (16), 2010293.

- (17) Lee, S. J.; Akopov, G.; Adeyemi, A. N.; Soto, E.; Wu, K.; Kovnir, K. IrSi<sub>3</sub>As<sub>3</sub>: A First Transition Metal Arsenide Non-Linear Optical Material. *J. Mater. Chem. A* **2023**, *11*, 11767.
- (18) Chen, J.; Lin, C.; Peng, G.; Xu, F.; Luo, M.; Yang, S.; Shi, S.; Sun, Y.; Yan, T.; Li, B.; Ye. N. BaGe<sub>2</sub>Pn<sub>2</sub> (Pn= P, As): Two Congruent-Melting Non-chalcopyrite Pnictides as Mid- and Far-Infrared Nonlinear Optical Materials Exhibiting Large Second Harmonic Generation Effects. *Chem. Mater.* **2019**, *31* (24), 10170-10177.
- (19) Sun, Y.; Chen, J.; Yang, S.; Li, B.; Chai, G.; Lin, C.; Luo, M.; Ye, N. LaSiP<sub>3</sub> and LaSi<sub>2</sub>P<sub>6</sub>: Two Excellent Rare-Earth Pnictides with Strong SHG Responses as Mid- and Far-Infrared Nonlinear Optical Crystals. *Adv. Opt. Mater.* **2021**, *9* (10), 2002176.
- (20) Akopov, G.; Mark, J.; Viswanathan, G.; J. Lee, S.; C. McBride, B.; Won, J.; A. Perras, F.; L. Paterson, A.; Yuan, B.; Sen, S.; N. Adeyemi, A.; Zhang, F.; Wang, C.-Z.; Ho, K.-M.; J. Miller, G.; Kovnir, K. Third Time's the Charm: Intricate Non-Centrosymmetric Polymorphism in LnSiP<sub>3</sub> (Ln = La and Ce) Induced by Distortions of Phosphorus Square Layers. *Dalton Trans.* **2021**, *50* (19), 6463–6476.
- (21) Chen, J.; Chen, H.; Xu, F.; Cao, L.; Jiang, X.; Yang, S.; Sun, Y.; Zhao, X.; Lin, C.; Ye, N. Mg<sub>2</sub>In<sub>3</sub>Si<sub>2</sub>P<sub>7</sub>: A Quaternary Diamond-like Phosphide Infrared Nonlinear Optical Material Derived from ZnGeP<sub>2</sub>. J. Am. Chem. Soc. **2021**, 143 (27), 10309–10316.
- (22) Narang, P.; Garcia, C. A. C.; Felser, C. The Topology of Electronic Band Structures. *Nat. Mater.* **2021**, *20* (3), 293–300.
- (23) Lee, S. J.; Won, J.; Wang, L.-L.; Jing, D.; Harmer, C. P.; Mark, J.; Akopov, G.; Kovnir, K. New Noncentrosymmetric Tetrel Pnictides Composed of Square-Planar Gold(I) with Peculiar Bonding. Chem. – Eur. J. 2021, 27 (26), 7383–7390.
- (24) Lee, S. J.; Viswanathan, G.; Carnahan, S. L.; Harmer, C. P.; Akopov, G.; Rossini, A. J.; Miller, G. J.; Kovnir, K. Add a Pinch of Tetrel: The Transformation of a Centrosymmetric Metal into a Nonsymmorphic and Chiral Semiconductor. *Chem. Eur. J.* **2022**, *28* (9), e202104319.
- (25) Yang, H.-D.; Ran, M.-Y.; Wei, W.-B.; Wu, X.-T.; Lin, H.; Zhu, Q.-L. The Rise of Infrared Nonlinear Optical Prictides: Advances and Outlooks. *Chem. Asian J.* **2021**, *16* (21), 3299–3310.
- (26) Chen, J.; Wu, Q.; Tian, H.; Jiang, X.; Xu, F.; Zhao, X.; Lin, Z.; Luo, M.; Ye, N. Uncovering a Vital Band Gap Mechanism of Pnictides. *Adv. Sci.* **2022**, *9* (14), 2105787.
- (27) Kaiser, P.; Jeitschko, W. Preparation and Crystal Structures of the Ternary Compounds Ag<sub>2</sub>SiP<sub>2</sub> and AuSiP. *Z. Für Naturforschung B* **1997**, *52* (4), 462–468.
- (28) *Inorganic Crystal Structure Database*. https://icsd.products.fiz-karlsruhe.de/ (accessed 2024-05-21).
- (29) *Prices of chemical elements*. https://en.wikipedia.org/wiki/Prices\_of\_chemical\_elements (accessed 2024-01-10).
- (30) Perrier, Ch.; Vincent, H.; Chaudouët, P.; Chenevier, B.; Madar, R. Preparation and Crystal Structure of a New Family of Transition Metal Phospho-Silicides. *Mater. Res. Bull.* **1995**, *30* (3), 357–364.
- (31) Perrier, Ch.; Kreisel, J.; Vincent, H.; Chaix-Pluchery, O.; Madar, R. Synthesis, Crystal Structure, Physical Properties and Raman Spectroscopy of Transition Metal Phospho-Silicides MSi<sub>x</sub>P<sub>y</sub> (M = Fe, Co, Ru, Rh, Pd, Os, Ir, Pt). *J. Alloys Compd.* **1997**, 262–263, 71–77.
- (32) Yu, T.; Wang, S.; Ruan, H.; Li, C.; Zhang, X.; Jia, N.; Zhang, J.; Tao, X. Flux Growth and Characterization of an FeSi<sub>4</sub>P<sub>4</sub> Single Crystal. *RSC Adv.* **2017**, *7* (76), 47938–47944.

- (33) Akopov, G.; Viswanathan, G.; Hewage, N. W.; Yox, P.; Wu, K.; Kovnir, K. Pd and Octahedra Do Not Get along: Square Planar [PdS<sub>4</sub>] Units in Non-Centrosymmetric La<sub>6</sub>PdSi<sub>2</sub>S<sub>14</sub>. *J. Alloys Compd.* **2022**, 902, 163756.
- (34) Akopov, G.; Hewage, N. W.; Yox, P.; Viswanathan, G.; Lee, S. J.; Hulsebosch, L. P.; Cady, S. D.; Paterson, A. L.; Perras, F. A.; Xu, W.; Wu, K.; Mudryk, Y.; Kovnir, K. Synthesis-Enabled Exploration of Chiral and Polar Multivalent Quaternary Sulfides. *Chem. Sci.* **2021**, *12* (44), 14718–14730.
- (35) Kim, S.-B.; Cho, Y.-H; Lee, J.-M.; Jung, J.-G.; Lim, S. G. The Effect of Ultrasonic Melt Treatment on the Microstructure and Mechanical Properties of Al-7Si-0.35Mg Casting Alloys. *Korean J. Met. Mater.* **2017**, *55*(4), 240-246.
- (36) Patel, D. N.; Sutaria, M. P. Effect of Trace Rare Earth Er Addition on Microstructure and Tensile Properties of 319 Al-Si-Cu Alloy. *Int. J. Met.* **2022**, *16* (4), 2199–2209.
- (37) Kang, J.; Su, R.; Wu, D. Y.; Liu, C. H.; Li, T.; Wang, L. S.; Narayanaswamy, B. Synergistic Effects of Ce and Mg on the Microstructure and Tensile Properties of Al-7Si-0.3Mg-0.2Fe Alloy. *J. Alloys Compd.* **2019**, 796, 267–278.
- (38) Ono, S.; Hayakawa, H.; Nomura, K. Synthesis of Ln-Si-P (Ln = La, Ce, Pr) Ternary Compounds, *J. Chem. Soc. Jpn.* **1976**, *11*, 1700–1709.
- (39) Hayakawa, H.; Ono, S.; Kobayashi, A. The Crystal Structure of Cerium Silicon Triphosphide (CeSiP<sub>3</sub>), *J. Chem. Soc. Jpn.* **1978**, *9*, 1214–1220.
- (40) Pauling, L. The nature of the chemical bond and the structure of molecules and crystals: an introduction to modern structural chemistry. Cornell University Press, Ithaca, N.Y 1960.
- (41) Mark, J.; Dolyniuk, J.-A.; Tran, N.; Kovnir, K. Crystal and Electronic Structure and Optical Properties of AE<sub>2</sub>SiP<sub>4</sub> (AE = Sr, Eu, Ba) and Ba<sub>4</sub>Si<sub>3</sub>P<sub>8</sub>. *Z. anorg. allg. Chem.* **2019**, *645*, 242–247.
- (42) Haffner, A.; Weippert, V.; Johrendt, D. Polymorphism of Ba<sub>2</sub>SiP<sub>4</sub>. Z. anorg. allg. Chem. **2020**, 646, 120–124.
- (43) Haffner, A.; Johrendt, D. Synthesis, Crystal Structure, and Chemical Bonding of Ba<sub>2</sub>SiP<sub>4</sub>. Z. Z. anorg. allg. Chem. **2017**, 643 (21), 1717–1720.
- (44) Akopov, G.; Viswanathan, G.; Kovnir, K. Synthesis, Crystal and Electronic Structure of La<sub>2</sub>SiP<sub>4</sub>. *Z. Z. anorg. allg. Chem.* **2021**, *647*, 91–97.
- (45) Kaiser, P.; Jeitschko, W. The Rare Earth Silicon Phosphides LnSi<sub>2</sub>P<sub>6</sub> (Ln= La, Ce, Pr, and Nd). *J. Solid State Chem.* **1996**, *124* (2), 346–352.
- (46) Raymond, K. N.; Girolami, G. S. Pathological Crystal Structures. *Acta Crystallogr. Sect. C Struct. Chem.* **2023**, 79 (11), 445–455.
- (47) Bekaert, E.; Bernardi, J.; Boyanov, S.; Monconduit, L.; Doublet, M.-L.; Ménétrier, M. Direct Correlation between the <sup>31</sup>P MAS NMR Response and the Electronic Structure of Some Transition Metal Phosphides. *J. Phys. Chem. C* **2008**, *112* (51), 20481–20490.
- (48) Furo, I.; Bakonyi, I.; Tompa, K.; Zsoldos, E.; Heinmaa, I.; Alla, M.; Lippmaa, E. <sup>31</sup>P Nuclear Magnetic Resonance Knight Shift and Linewidth in Ni<sub>3</sub>P and Cu<sub>3</sub>P: A Magic-Angle Spinning Study. *J. Phys. Condens. Matter* **1990**, *2* (18), 4217.
- (49) Stinner, C.; Tang, Z.; Haouas, M.; Weber, Th.; Prins, R. Preparation and <sup>31</sup>P NMR Characterization of Nickel Phosphides on Silica. *J. Catal.* **2002**, *208* (2), 456–466.

- (50) Kurtz, S. K.; Perry, T. T. A Powder Technique for the Evaluation of Nonlinear Optical Materials. *J. Appl. Phys.* **2003**, *39* (8), 3798–3813.
- (51) Gonze, X.; Lee, C. Dynamical Matrices, Born Effective Charges, Dielectric Permittivity Tensors, and Interatomic Force Constants from Density-Functional Perturbation Theory. *Phys. Rev. B* 1997, 55 (16), 10355–10368.
- (52) Perdew, J. P.; Wang, Y. Accurate and Simple Analytic Representation of the Electron-Gas Correlation Energy. *Phys. Rev. B* **1992**, *45* (23), 13244–13249.
- (53) Krukau, A. V.; Vydrov, O. A.; Izmaylov, A. F.; Scuseria, G. E. Influence of the Exchange Screening Parameter on the Performance of Screened Hybrid Functionals. *J. Chem. Phys.* 2006, 125 (22), 224106.
- (54) Clark, D. J.; Zhang, J.-H.; Craig, A. J.; Weiland, A.; Brant, J. A.; Cho, J. B.; Kim, Y. S.; Jang, J. I.; Aitken, J. A. The Kurtz-Perry Powder Technique Revisited: A Case Study on the Importance of Reference Quality and Broadband Nonlinear Optical Measurements Using LiInSe<sub>2</sub>. J. Alloys Compd. 2022, 917, 165381.
- (55) Qi, L.; Chen, H.; Chen, Y. Third Order Tensors in Physics and Mechanics. In *Tensor Eigenvalues and Their Applications*; Qi, L., Chen, H., Chen, Y., Advances in Mechanics and Mathematics, Eds., Springer: Singapore, **2018**, pp 207–248.
- (56) Jackson, A.; Ohmer, M.; Leclair, S. Relationship of the Second Order Nonlinear Optical Coefficient to Bandgap in Inorganic Non-Centrosymmetric Crystals. *Core Sch.* 1995.
- (57) Lee, M.-H.; Yang, C.-H.; Jan, J.-H. Band-Resolved Analysis of Nonlinear Optical Properties of Crystalline and Molecular Materials. *Phys. Rev. B* **2004**, *70* (23), 235110.
- (58) Lambrecht, W. R. L.; Rashkeev, S. N. From Band Structures to Linear and Nonlinear Optical Spectra in Semiconductors. *Phys. Status Solidi B* **2000**, *217* (1), 599–640.
- (59) Sipe, J. E.; Ghahramani, E. Nonlinear Optical Response of Semiconductors in the Independent-Particle Approximation. *Phys. Rev. B* **1993**, *48* (16), 11705–11722.
- (60) Wu, K.; Zhang, B.; Yang, Z.; Pan, S. New Compressed Chalcopyrite-like Li<sub>2</sub>BaM<sup>IV</sup>Q<sub>4</sub> (M<sup>IV</sup> = Ge, Sn; Q = S, Se): Promising Infrared Nonlinear Optical Materials. *J. Am. Chem. Soc.* **2017**, *139* (42), 14885–14888.

